Dovepress

Open Access Full Text Article

ORIGINAL RESEARCH

Mitochondrial Targeted Cerium Oxide Nanoclusters for Radiation Protection and Promoting Hematopoiesis

Luxun Yang[1,*], Haiying Ran[2,*], Yaru Yin[1], Jing Liu[1], Binghui Lu[1], Xi Ran[3], Shenglin Luo[1], Weidong Wang[4], Zhangyou Yang[5], Rong Li[1]

[1]Institute of Combined Injury, National Key Laboratory of Trauma and Chemical Poisoning, Army Key Laboratory of Nanomedicine, Department of Military Preventive Medicine, Army Medical University, Chongqing, 400038, People's Republic of China; [2]Biomedical Analysis Center, Army Medical University, Chongqing, 400038, People's Republic of China; [3]Department of Medical Laboratory, Xinqiao Hospital, Army Medical University, Chongqing, 400037, People's Republic of China; [4]Department of Radiation Oncology, Sichuan Cancer Hospital, Chengdu, 610041, People's Republic of China; [5]Chongqing Key Laboratory for Pharmaceutical Metabolism Research, Chongqing Pharmacodynamic Evaluation Engineering Technology Research Center, College of Pharmacy, Chongqing Medical University, Chongqing, 400016, People's Republic of China

*These authors contributed equally to this work

Correspondence: Zhangyou Yang, Chongqing Medical University, No. 1, Yixueyuan Road, Chongqing, 400016, People's Republic of China, Email yangzhangyou@cqmu.edu.cn; Rong Li, Army Medical University, No. 30, Gaotanyan Street, Chongqing, 400038, People's Republic of China, Tel +86-13883996627, Fax +8623-68753127, Email lrong361@126.com

Purpose: Mitochondrial oxidative stress is an important factor in cell apoptosis. Cerium oxide nanomaterials show great potential for scavenging free radicals and simulating superoxide dismutase (SOD) and catalase (CAT) activities. To solve the problem of poor targeting of cerium oxide nanomaterials, we designed albumin-cerium oxide nanoclusters (TPP-PCNLs) that target the modification of mitochondria with triphenyl phosphate (TPP). TPP-PCNLs are expected to simulate the activity of superoxide dismutase, continuously remove reactive oxygen species, and play a lasting role in radiation protection.

Methods: First, cerium dioxide nanoclusters (CNLs), polyethylene glycol cerium dioxide nanoclusters (PCNLs), and TPP-PCNLs were characterized in terms of their morphology and size, ultraviolet spectrum, dispersion stability and cellular uptake, and colocalization Subsequently, the anti-radiation effects of TPP-PCNLs were investigated using in vitro and in vivo experiments including cell viability, apoptosis, comet assays, histopathology, and dose reduction factor (DRF).

Results: TPP-PCNLs exhibited good stability and biocompatibility. In vitro experiments indicated that TPP-PCNLs could not only target mitochondria excellently but also regulate reactive oxygen species (ROS)levels in whole cells. More importantly, TPP-PCNLs improved the integrity and functionality of mitochondria in irradiated L-02 cells, thereby indirectly eliminating the continuous damage to nuclear DNA caused by mitochondrial oxidative stress. TPP-PCNLs are mainly targeted to the liver, spleen, and other extra-medullary hematopoietic organs with a radiation dose reduction factor of 1.30. In vivo experiments showed that TPP-PCNLs effectively improved the survival rate, weight change, hematopoietic function of irradiated animals. Western blot experiments have confirmed that TPP-PCNLs play a role in radiation protection by regulating the mitochondrial apoptotic pathway.

Conclusion: TPP-PCNLs play a radiologically protective role by targeting extramedullary hematopoietic organ-liver cells and mitochondria to continuously clear ROS.

Keywords: radioprotective effect, ceria nanoclusters, mitochondria targeting, oxidative stress, superoxide dismutase

Introduction

Ionizing Radiation (IR) produces free radicals and toxic substances when it passes through the cells. Reactive oxygen species (ROS) can attack cellular macromolecules, such as DNA, resulting in DNA breaks, while ROS cause oxidative stress, leading to mitochondrial damage and dysfunction. Mitochondrial oxidative stress is a primary cause of cell death and apoptosis. Anti-radiation drugs are mainly concentrated in sulfur compounds, hormones, plant drugs, cytokines, and

6463

other molecules. However, these drugs have certain limitations, such as weak biocompatibility and poor targeting.[1] In addition, traditional anti-radiation drugs to effectively accumulate in the target area of radiation injury, resulting in serious off-target effects and significantly reduced efficacy. Therefore, finding a new radiation protection strategy that combines effective drugs with therapeutic targets is an urgent and difficult problem.

It is widely established that mitochondrial ROS plays an important role in DNA repair after radiation damage. Compared with nuclear DNA, mtDNA is more sensitive to radiation and free radical damage due to its lack of histone protection and effective self-repair ability.[2] Mitochondria are the power source of cells, and supply cells with adenosine triphosphate (ATP) through oxidative phosphorylation process to maintain cellular energy homeostasis. ROS byproducts generated during the radiation process can cause mitochondrial dysfunction, such as blocked ATP synthesis, DNA mutation, and promotion of intrinsic apoptotic pathways. The continuous generation of free radicals in the mitochondria in the late stage can be mediated by the nucleus and cause sustained secondary free radical damage to DNA in the nucleus, resulting in far-late damage to radiation. MnSOD overexpression in mitochondria has been reported to stabilize mitochondrial membrane potential (MMP), increase ATP levels, reduce radiation-induced free radical damage, and inhibit radiation-induced apoptosis.[3] However, when superoxide dismutase (SOD) eliminates O2 produced by mitochondria, it also produces secondary H_2O_2 and free radicals. Only by simultaneously increasing the expression of SOD and CAT in mitochondria at the same time can the radiation protection ability be enhanced.[2] How to target mitochondria reasonably and effectively to regulate the activity of various enzymes, such as SOD and CAT, is a difficult problem.

Ceria nanomaterials, owing to the coexistence and mutual transformation of Ce^{3+} and Ce^{4+} on their surfaces, are recyclable, and there are mainly two types of simulated enzyme activities (simulated superoxide dismutase and catalase), which can effectively clear a variety of active free radicals. They exhibit the high efficiency, long-term and renewable ability of scavenging free radicals.[4–7] We also synthesized bovine serum albumin(BSA) coated cerium dioxide nanoclusters (CNLs), nanoparticles (CNPs) and nanochains (CNHs) in a controlled manner, showing that these cerium oxide compounds have a good protective effect on the radiation damage of human hepatocytes L-02. Among them, CNLs show the highest enzyme activity owing to their high specific surface area and broad application prospects.[8] However, their lack of targeting ability and biocompatibility limits their further application in the field of radiation protection.

The mitochondrial-targeting molecule triphenylphosphine (TPP) is a lipophilic cation with hydrophobic characteristics that can target the mitochondria to take advantage of their negative membrane potential. As indicated, the business end of TPP is a parent molecule containing a nitroxide group that exhibits SOD mimetic activity, a phenolic hydroxyl group (OH) with a chain-breaking radical scavenging ability.[9] Polyethylene glycol (PEG) modification can prolong half-life, reduce immunogenicity and enhance physical, chemical and biological stability.[10] Our previous studies have shown that PEG-modified cerium dioxide nanoparticles (CNPs) have a good protective effect against radiation damage in human hepatocytes, because PEGylated modification improves the chemical stability of CNPs and reduces the biological toxicity.[9]

Mitochondrial oxidative stress is an important factor in cell apoptosis and mitochondria can serve as important potential targets for radiation protection, so mitochondria-targeted radiation may be a promising therapeutic approach for radioprotection. The current anti-radiation drugs have poor radiation protection effects due to poor water solubility, stability, and biological compatibility. And it does not have a targeting effect. To solve the problem of poor targeting and stability of cerium oxide nanomaterials, we designed an mitochondria-targeted ceria nanoclusters (TPP-PCNLs) targeting mitochondria through polyethylene glycol mediated triphenyl phosphate (TPP) modification (Scheme 1). The radiation protection mechanism of TPP-PCNLs is based on targeting mitochondria while continuously clearing free radicals, efficiently simulating SOD enzyme activity, improving the damage of excessive oxidative stress to mitochondria, reducing indirect DNA damage and cell apoptosis, and achieving the long-lasting radiation protection effect of TPP-PCNLs. Finally, this new strategy may be a candidate for improving the patients' quality of life and ameliorating the late effects of radiation damage in the future.
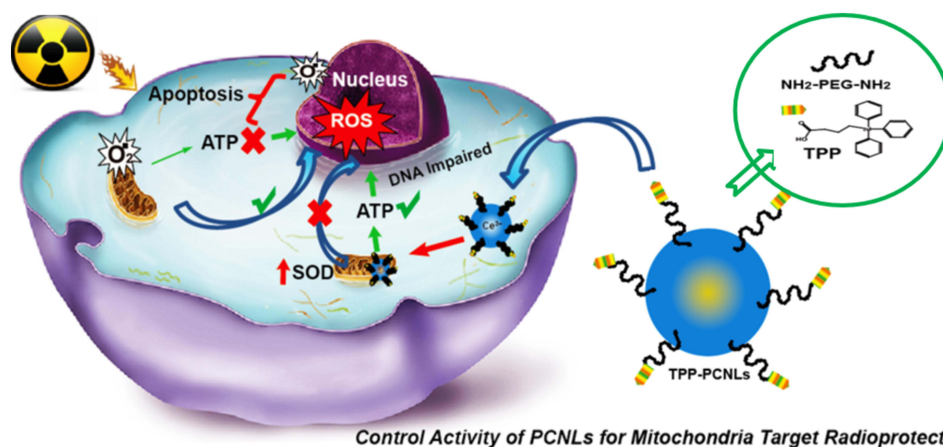
Scheme 1 Schematic diagram based on mitochondria targeted biocompatibility ceria nanoclusters used for radioprotection and promoting hematopoiesis.

Materials and Methods

Materials

All chemicals were purchased from Sigma-Aldrich and used as received. Ultrapure Millipore water (18.2 M Ω) was used for the experiments. All glassware was washed with chromic acid solution and rinsed with ultrapure water. (Caution: Chromic acid lotion is a highly corrosive oxidizing agent that should be handled with great care).

Cerium (III) nitrate hexahydrate (99%), Cy3, Triphenyl Phosphate Free of Phenol (TPP), N-hydroxysuccinimide (NHS), N-(3-dimethylamino-propyl)-N-ethylcarbodiimide (EDC), dimethyl sulfoxide (DMSO), and bovine serum albumin (BSA) were purchased from Sigma-Aldrich (St. Louis, MO, USA). Fetal bovine serum (FBS), penicillin-streptomycin, and Dulbecco's modified Eagle's medium (DMEM) were purchased from Gibco Life Technologies (Carlsbad, CA, USA). The Cell Counting Kit-8 (CCK-8) was purchased from Dojindo (Kumamoto, Japan), and Calcein AM and PI were purchased from Sangon Biotech (Shanghai, China). Glutathione Peroxidase (GPX), glutathione (GSH), MMP assay kit with JC-1, ATP Assay Kit and ROS Kit (DCFH-DA) were purchased from Biyuntian Biotechnology Co. Ltd. (Shanghai, China). Malondialdehyde (MDA) assay kit was purchased from Nanjing Jiancheng Bioengineering Institute (Nanjing, China). Mito-Tracker was purchased from Santa Cruz Biotechnology (Dallas, Texas). Mito-SOX Red Mitochondrial Superoxide Indicator was purchased from Yesen Technology (Shanghai, China). Annexin V-FITC was purchased from BD Pharmingen (Franklin Lakes, NJ, USA). PVDF membrane, protein marker, goat anti-rabbit IgG secondary antibody, SDS-PAGE prefabricated adhesive, ECL development light-producing solution, primary antibody diluent, secondary antibody diluent, rapid sealing solution, and β-actin antibody (1:500 dilution) were purchased from Beyotime Biotechnology (Shanghai, China). Caspase-3 primary antibody (1:500 dilution), Caspase-9 primary antibody (1:500 dilution), Bax (1:2000 dilution), and Bcl-2 (1:2000 dilution) were purchased from Proteintech Group, Inc. (Chicago, IL, USA). All the chemical reagents were of analytical grade.

Synthesis of PCNLs and TPP-PCNLs and Corresponding Cy3 and ICG Markers

PCNLs and TPP-PCNLs were labeled with Cy3 and their colocalization in the cell was observed using a confocal laser. PCNLs and TPP-PCNLs were labeled with ICG, and their targeted properties in tissues and organs were observed using in vivo imaging.

Synthesis of Albumin Coated CNLs, Cy3-CNLs or CNLS-ICG

At room temperature, 125 mg of Bovine Serum Albumin (BSA) was dissolved in 4 mL of ultrapure water, stirred, and dispersed. 250μL 0.1 M cerium nitrate hexahydrate solution was added to the solution. After reacting for 15 min, 400μL of 1 M KOH solution was added. After reacting for 15 min, CNLs were dialyzed in ultrapure water for 24h, centrifuged, and purified. Cy3-labeled ceria nanoclusters (CNLs-Cy3) or CNLs-ICG were synthesized using the same methods as above, except adding 50μL of 1mM Cy3 DMSO or 200μL (5 mmol) ICG solution was added to the BSA solution. The Ce content was determined using inductively coupled plasma mass spectrometry (ICP-MS) (Agilent 7500cx, Santa Clara, CA, USA).

Synthesis of PEGylated Ceria Nanoclusters (PCNLs), Cy3-PCNLs or PCNLs-ICG

15 mg EDC and 15 mg NHS carboxylic acid activator were added to 4 mL 0.2 mg /mL CNLs, or Cy3-CNLs, or CNLs-ICG solution, and 30 mg aminoated polyethylene glycol (NH2-PEG4000-NH2) was added to the above reaction system after the activation reaction for 15 min. The pH was adjusted to approximately 9 using triethylamine. The reaction was continued for 24 h, and dialysis purification was performed for 24 h to obtain the PCNLs, Cy3-PCNLs, and PCNLs-ICG.

Synthesis of Mitochondrial Targeting Multifunctional Ceria Nanoclusters (TPP-PCNLs), Cy3- TPP-PCNLs or TPP-PCNLs -ICG

Firstly, 5 mg TPP was dissolved in 500μL DMSO solution, and 10 mg EDC/NHS was added to it for activation for 4 h; then they were added to 0.2 mg/ mL PCNLs or PCNLs-Cy3 or PCNLs-ICG system for 24 h. TPP-PCNLs, TPP-PCNLs-Cy3, and TPP-PCNLs-ICG were obtained via dialysis and purification with ultrapure water. The were stored in refrigerator at 4°C until further use.

Materials Characterization

The ceria nanoclusters were characterized using high-resolution transmission electron microscopy (HR-TEM) (Tecnai G2 F20 S-TWIN, FEI Corporation, Oregon, USA) at an accelerating voltage of 200 kV. Dry nanoparticle samples were X-ray diffracted using an X-ray diffractometer (XRD) (Persee XD3, Beijing, China) under Cu NF radiation at 36kv and 20ma.Dynamic light scattering (DLS) of the nanomaterials was performed using a Zeta PALS analyzer (Brookhaven, USA). The nanomaterials were dried for 24 h in a freeze-dryer (EYELA FDU-2100, Tokyo, Japan). A Zetasizer (ZEN3600, Malvern, UK) was used to measure the zeta potential of the synthetic compound three times in deionized water at 25°C. The characterization of the CNLs, PCNLs, and TPP-PCNLs was determined by a UV-NIR spectro-photometer (UV3600 Scanning Spectrophotometer, Shimadzu, Japan). Fourier transform infrared (FT-IR spectroscopy) (NICOLET6700, Thermo Field, USA) was used to obtain the infrared spectra of the synthesized compounds. X-Ray photoelectron spectroscopy (XPS) experiments were performed using a multipurpose surface analysis system (Scientific Escalab 250, Thermo Fisher Scientific, UK) with argon sputtering.

SOD and CAT Simulated Activity: Riboflavin-Nitrogen Blue Tetrazole (NBT) Method

A solution containing 800μL ethylenediamine-tetraacetic acid solution (0.1M), 300 μL NBT solution (2 mM), 200 μL riboflavin solution (0.6 mM) and 11.4 mL phosphate solution was mixed under light-proof conditions. 50μL Ceria nanomaterials was mixed with 100μL detection solution. The mixture was shaken in a 96-well plate for 1 min under free conditions. The plate was then placed under an incandescent light for 10 min. Inhibition was calculated based on the decrease in absorbance at 560 nm.

The sample and standard were added to a Petri dish, the stop solution was added to the sample control well and incubated at 25°C for 5 min. The H_2O_2 solution was added to the wells, incubated at 25°C for 30 min, and the stop solution was added. The developer was added, mixed, incubated at 25°C for 10 min, and analyzed using a microplate reader.

Hemolysation Test

Mouse blood was collected, centrifuged at $1000 \times$ g for 10 min to remove the supernatant, and then resuspended in PBS (pH=7.4) three times, and 100μL was added to the EP tube. Subsequently, 900μL of deionized water was added to the positive control group, 900μL of PBS was added to the negative control group, and add 900 microliters of appropriate concentration of CNLs, PCNLs and TPP-PCNLs to the sample group to achieve final concentrations of 0.1, 1 and 10 μg/mL. After mixing, EP tube was incubated on a shaking table at 37°C for 120 min, then centrifuged at 10^3g for 10 min, and EP tube photos were collected. The absorbance at 540 nm was measured using an enzyme-labeled instrument, and hemolysis of each group was calculated according to the following formula: hemolysis rate (%) = (OD sample − OD negative control group)/(OD positive control group − OD negative control group) × 100%.

Irradiation

Cell and animal radiation are irradiated with X-ray irradiator (X-RAD 320, PXI, USA) with a dose rate of 1.2 G y/ min from Institute of Combined Injury, Army Medical University, to evaluate the protective effect of cerium nanomaterials on radiation induced injury.

In Vitro Studies

Cell

Normal human liver (L-02) Cells were purchased from the cell bank of the Chinese Academy of Sciences (Shanghai, China) and maintained in high-glucose DMEM containing 1% penicillin–streptomycin and 10% FBS. The cells were seeded in 6-well plates at 37°C in a 5% CO_2 humidified chamber. Trypsin digestion method (0.25% trypsin) was used for passaging every other day, and log-phase cells were used for the experiment. Cells were irradiated using an X-ray irradiator at a dose rate of 1.2 Gy/min.

Cellular Uptake

L-02 cells were seeded in Petri dishes and incubated with PCNLs and TPP-PCNLs (40μg/ mL) for 1, 4, 12, and 24 h. Cells were collected, washed three times with PBS (pH 7.4), and coordinated to 5×10^5 cells/mL. Concentrated nitric acid (500μL) was added to the samples, which were hydrolyzed at 70°C for 5h. The Ce concentration was tested using ICP-MS.[9]

Subcellular Colocalization

The subcellular colocalization of cerium nanomaterials was evaluated using confocal fluorescence microscopy to evaluate the mitochondrial-targeting effect. For confocal microscopy, 1×10^4 cells were incubated with Cy3 labeled PCNLs and TPP-PCNLs at a concentration of 1 μg/mL for 4 h. After being washed with PBS, the cells were incubated with Mito-Tracker (150 n M, 30 min at 37°C). The cells were washed, fixed with 10% formalin, and incubated with DAPI (1 mg/mL) for 10 min. Finally, the cells were washed and visualized under a confocal microscope (TCS-SP5; Leica, Mannheim, GER).The excitation wavelength of the microscope was 550 nm and the emission wavelength was 570 nm.[9]

Cell Viability Analysis (CCK-8 Assay)

For the cytotoxicity assay, cells were incubated with 0, 0.01, 0.1, 1, and 10μg/ mL of PCNLs or TPP-PCNLs for 72 h. Cell viability was determined by CCK-8 assay using a kit.

To observe the radiation protection effect, cells were pretreated with concentrations of 0, 0.01, 0.1,1, 10 μg/ mL of PCNLs or TPP-PCNLs for 24 h, and then exposed to 6Gy X-rays. Cell viability was measured 72 h post-Irradiation using the CCK-8 assay. In subsequent cell experiments, we selected PCNLs or TPP-PCNLs pretreated cells at concentrations of 0, 0.01, 0.1, and 1μg/ mL. The concentrations of PCNLs and TPP-PCNLs used in later cell experiments were the same, unless otherwise specified.

Cellular Mechanism of Radiation Protection of TPP-PCNLs

Cell Processing

L-02 cells were inoculated into 6-well plates (1×10^3 cells per well), pretreated with 0, 0.01, 0.1 and 1μg/mL PCNLs or TPP-PCNLs for 12 h, and then irradiated with 6 G y X-ray.

Transmission Electron Microscope Ultrastructural Imaging

L-02 cells were inoculated into 6-well plates (2×10^6 cells per well), pretreated with 1μg/mL PCNLs or TPP-PCNLs for 12 h, and irradiated with 6 Gy X-rays. Trypsined cells were fixed at room temperature with 2.5% glutaraldehyde in 0.1 M sodium cacodylate buffer, fixed with 1% osmium tetroxide in the same buffer, dehydrated in increasing concentrations of ethanol, and embedded in epoxy resins. Thin sections were observed under a transmission electron microscope (Tecnai G2F20S-TWIN, Philips-FEI, Hillsboro, OR, USA).

Mitochondrial ATP Assay

Treated L-02 cells were incubated for 72h. After rinsing with PBS, the treated cells were harvested. Mitochondrial ATP levels were determined using an ATP assay and measured using a luminometer (Olympus DP80; Shinjuku-ku, Tokyo, Japan).

MMP Assay

Treated L-02 cells were incubated for 72h. After rinsing with PBS, the treated cells were harvested. The JC-1 dye solution (1 mL) was added, incubated at 37°C for 20 min, washed twice with JC-1 buffer, and observed under a fluorescence microscope (DP80; Olympus). ImageJ software (Image J 1.51, NIH, USA) was used for the quantification of fluorescence intensity.

The Intracellular ROS and Mitochondrial Superoxide Levels Assay

The fluorescent dyes H2DCF-DA and Mito-SOX Red were used to measure the intracellular ROS and mitochondrial superoxide levels, respectively, as previously described. Treated L-02 cells were incubated for 4 h. After being rinsed with PBS, cells were incubated with 5×10^{-6} M H2DCF-DA or Mito-SOX Red for 20 min at 37°C. ROS and mitochondrial superoxide levels in the cells were observed using fluorescence microscopy at 480 nm excitation and 525 nm emission wavelengths. ImageJ software was used for fluorescence intensity quantification.

Clonal Survival Analysis

The treated L-02 cells were cultured for 10 days until colonies were clearly visible. Colonies were fixed with 4% paraformaldehyde and stained with 0.5% crystal violet. Under a microscope, all colony images were representative of one of three independent experiments, and the number of clones in each group was counted.

Calcein AM and Propidium Iodide (PI) Staining

The radioprotective effects of PCNLs and TPP-PCNLs on L-02 cells were further verified using Calcein AM and PI co-staining. Treated L-02 cells were incubated for 72 h. After being rinsed with PBS, cells were incubated with Calcein AM/PI for 20 min at 37°C. The probe was loaded and visualized using a fluorescence microscope.[9] The fluorescence intensity was quantified using the ImageJ software (ImageJ 1.51, NIH, USA).

Alkaline Single-Cell Gel Electrophoresis

DNA damage was detected by alkaline single-cell gel electrophoresis. The cell suspension was added to low melting point-agarose at 37°C, and 60μL of the mixture was placed on a microscope slide coated with one dried layer of 1% normal agarose in PBS. The slides were immersed 1 h in cold lysis buffer at 4°C in the dark. The slides were then immersed in a pre-cooled electrophoresis buffer for 30 min and electrophoresis was performed at 22 V/300 mA for 25 min. After electrophoresis, the slides were rinsed thrice for 5 min with PBS and stained with ethidium bromide (100μL per slide, 2.5μg/mL). Finally, cells were washed and visualized under a fluorescence microscope.The degree of DNA damage was analyzed using the Comet Assay Software (CASP software, Beijing Biliang Technology Co., LTD., China) and assessed by the percentage of DNA in the comet tail (tail DNA%).

Flow Cytometric Analysis of Apoptosis

Apoptosis was determined using the Annexin V-FITC staining assay. The treated L-02 cells were incubated for 72h, and collected, and stained with Annexin V-FITC/PI apoptosis detection kit solution at room temperature for 15 min. Finally, the cells were analyzed using flow cytometry (BD FACS Calibur, East Rutherford, NJ, USA).

Western Blotting

L-02 cells were inoculated into 6-well plates (1×10^6 cells per well), pretreated with 0, 1μg/mL TPP-PCNLs for 12 h, irradiated with 6Gy X-rays, and incubated for another 72 h. Treated cells were harvested and washed. Western blotting was performed as described previously.[9] Extraction of total protein was extracted from the cells using routine procedures. All protein samples were mixed with SDS-PAGE loading buffer, heated to 95°C for 10 min, separated on 8–12% SDS-PAGE gels, electrotransferred to polyvinylidene fluoride membranes, and blocked with blocking buffer for 1 h. Subsequently, samples were incubated overnight at 4 °C with the following primary antibodies: Bax, Bcl-2, Caspase-3, Caspase-9, and anti-β-actin. Appropriate secondary antibodies were selected and incubated with membranes for 2 h at room temperature.

The blot bands were visualized using ECL reagent. Non-saturated bands were selected for densitometric quantification using the ImageJ software (Image J 1.51, NIH, USA).

In vivo Studies

Animals: 8 weeks healthy male BALB/c mice (18–22 g) were purchased from the Experimental Animal Center of the Army Medical University. All mice received adaptive feeding to accommodate the environment for 1 week. The study design and all animal experimental procedures were performed in accordance with the Guide and Use of Laboratory Animals (Institute of Laboratory Animal Resources), and Animal treatment and which was approved by the Ethics Review Committee for Animal Experimentation at the Army Medical University (Animal Ethics Statement AMUWE2020718). feeding conditions were: ambient temperature, 24±1°C; relative humidity, 50±5%; light and dark cycle, 12/12 h.

Live Imaging of Small Animals

Male BALB/c mice (eight weeks old, 20–22 g) were obtained from Animal Center of Army Medical University. There is an important correlation between the radiation-protective effect of nanomaterials, blood circulation time, and organ distribution. After ICG (λ_{ex} = 790 nm; λ_{em} = 810 nm) loading, the distribution of CNLs, PCNLs, and TPPCNLs in the organs was observed using a small-animal living imager to determine whether they targeted hematopoietic organs. Male BALB/c mice were injected with 4 mg/kg ICG, PCNL-ICG, or TPP-PCNL-ICG through the tail vein for fluorescence imaging at 0h, 2h, 5h, 8h, 12h and 24h. During imaging, mice were anesthetized with isoflurane gas and then placed in a prone position in the camera obscura of the small Animal Multispectral imaging system (Viber Lourmat, France) to record whole-body images of the fluorescence emission of these cerium nanomaterials. 24h after injection, the mice were sacrificed, the heart, liver, spleen, lung, and kidney were removed, and the organs were imaged to analyze the distribution of the fluorescent cerium nanomaterials.

The Distribution of Cerium Nanomaterials in Various Organs

Male BALB/c mice (eight weeks old, 20–22 g) were obtained from Animal Center of Army Medical University. The distribution of cerium nanomaterials in various organs was analyzed using ICP-MS to determine whether they were mostly distributed in the radiation-sensitive organs. Fifteen healthy adult male BALB/c mice aged eight weeks were divided into three major groups: CNLs, including CNLs group, and TPP-PCNLs. After 10 mg/kg of CNLs, PCNLs, and TPP-PCNLs was injected into the tail vein, blood samples from the inner canthus vein of mice were collected at 0.25, 1, 2, 4, 12, 24, 48 h. The Ce content of the serum was analyzed using ICP-MS (n=5). After 48 h, heart, liver, spleen, lung, and kidney tissues from each group were collected. After microwave digestion, the Ce content was analyzed using ICP-MS.

Determination of Dose Reduction Factor (DRF) for TPP-PCNLs

Male BALB/c mice (eight weeks old, 20–22 g) were obtained from Animal Center of Army Medical University. To calculate the DRF value of TPP-PCNLs, the LD50/30 values of BALB/c mice exposed to radiation and the LD50/30 value of mice exposed to TPP-PCNLs under prophylactic administration were determined. To determine the optimal radiation dose, the effects of different doses of radiation (4, 6, 6.5, 7, 7.5, 8, 10, 12 Gy) on the 30-day survival rate of BALB/c mice were first evaluated, which provided the basis for calculating LD50/30 (IR). To evaluate the toxicity of TPP- PCNLs in mice, TPP- PCNLs at doses of 4, 6, 8,10,12,14 mg/kg were used to observe the 30 day survival rate. To determine the optimal concentration and the LD50/30 (TPP-PCNLs) values, TPP-PCNLs were administered prophylactically 12 h before irradiation, 180 BALB/c mice were randomly divided into nine groups: 1) At a radiation dose of 6 Gy, 4, 6, and 10 mg/kg TPP-PCNLs were administered; 2) At a radiation dose of 6, 6.5, 7, 8, 10 and 12 Gy, 10 mg/kg TPP-PCNLs were administered. The 30-day survival rate was determined, and the DRF value of TPP-PCNLs was calculated using formula (1):

$$DRF(TPP-PCNLs) = \frac{LD_{50/30}(TPP-PCNLs)}{LD_{50/30}(IR)} \tag{1}$$

The LD50/30 value is calculated through probit analysis based on radiation dose and survival rate.

Bodyweight and Mortality of Irradiated Mice

Male BALB/c mice (eight weeks old, 20–22 g) were obtained from Animal Center of Army Medical University. Eighty BALB/c mice were randomly divided into four groups: (1) control group "(IR(-)", normal mice without any treatment); (2) TPP-PCNLs group (mice are treated with TPP-PCNLs only); (3) Irradiation group ("IR (+)", mice are subjected to 6 G y doses of irradiation alone); (4) "TPP-PCNLs + IR (+)" group (mice were pretreated with TPP-PCNLs before irradiation) (n=20). Methods of administration: Twelve hours before irradiation, saline solution or a 10 mg/kg dose of TPP-PCNLs were injected into the tail vein of each group mice, but control group mice without any treatment.Body weight (g)(n=10) and mortality (n=20) were recorded at seven time-points: 1, 3, 6, 9, 14, 21, and 30 days after injury.

Determination of Liver Lipid Peroxidase Content and Antioxidant Enzyme

Three days after treatment, the liver tissue was harvested and the residual blood was washed with normal saline. The homogenate was placed in an ice bath and centrifuged at 4000 r/min for 10 min. The supernatant was collected and malondialdehyde (MDA), glutathione (GSH), and glutathione peroxidase (GP-x) activities were determined.

Determination of Red Blood Cells (RBCs), White Blood Cells (WBCs) and Platelets (PLTs) in the Blood Circulation

Venous blood specimens (μL) were collected from groups 1, 3, 6, 9, 14, and 21 d after injury.[8] The blood specimens were diluted with 130μL of heparin sodium solution and used for the automatic counting of red blood cells (RBCs), white blood cells (WBCs), and platelets (PLTs) on a blood cell analyzer (Sysmex, Japan) (n= 8/group).

Bone Marrow Nuclear Cells (BMNCs) Counting of Bone Marrow

The left femurs were obtained from the mice in each group seven days after irradiation (n=8/group) and thoroughly rinsed with PBS. The femoral heads were cut from both ends, and bone marrow cells (BMCs) were thoroughly flushed with 1640 medium. The cells were filtered through a 200-mesh sieve to obtain a single-cell suspension, and the bone marrow nucleated cells (BMNCs) were counted under an inverted microscope.

Count of Splenic Nodules (CFU-S)

The number of splenic nodules reflected the recovery of hematopoietic function in irradiated mice. Eight days after irradiation, mice were euthanized using the cervical dislocation method. The spleen was removed and fixed in Bouin's solution for 30 minutes. Gray nodules on the entire splenic surface were observed under a magnifying glass and counted.

Hematoxylin-Eosin Staining

At three days after irradiation, the bone marrow was small in the testis, liver, kidney, heart, spleen, and lungs obtained from the mice of each group (n=8/group). Seven days after irradiation, bone marrow was obtained from mice in each group (n=8/group). The sectioned specimens were stained with hematoxylin and eosin H&E (and observed under an inverted microscope to examine pathological changes.

Statistics

Unless otherwise indicated, data are expressed as the mean± standard error of the mean (SEM). difference in 30-d survival rates between the control and experimental groups were analyzed using a two-tailed Fisher's test. Other parameters, such as body weight change, peripheral hemogram, and cell viability, were compared using a one-way ANOVA with multiple comparisons. The LD50/30 values used for DRF determination were computed by probit analysis, and were given in Gy. Differences between two groups were assessed using Student's unpaired t-test. Differences were considered statistically significant at $P<0.05$.

Results

Synthesis and Characterization of TPP-PCNLs

As shown in Figure 1A, ceria nanoclusters (CNLs) were first obtained by albumin-mediated synthesis, and then mitochondria-targeted ceria nanoclusters (TPP-PCNLs) were obtained via PEGylation-mediated mitochondrial-targeted molecular modification. transmission electron microscope (TEM) and protein negative staining analysis showed that the core size of PCNLs (Figure 1B) and TPP-PCNLs (Figure 1D) was approximately 2 nm and evenly distributed, and the protein was approximately 10nm (Figure 1C and E) and evenly distributed, the outer protein shell was approximately 4 nm. Dynamic Light Scattering (DLS) analysis showed that the hydration particle size of TPP-PCNLs (~30 nm) was larger than that of PCNLs (~ 20 nm), both of which had good uniformity and could be absorbed into cells through endocytosis (Figure 1F). DLS analysis showed that TPP-PCNLs had good chemical stability in both PBS and PBS plus serum (PBS + 10% FBS) at 0–8 days under physiological conditions (Figure 1G). This may be due to the special physicochemical structure of BSA, and PEGylation could effectively maintain the chemical stability of nanoclusters under physiological conditions. More importantly, the disulfide bond structure of BSA can effectively maintain the Ce^{3+}/Ce^{4+} valence distribution ratio on the surface of ceria nanoclusters, which is beneficial for maintaining their biological activity. The UV spectrum Results showed that after loading the mitochondrial-targeting molecule TPP, the nanomaterial exhibited the characteristic absorption peak of TPP at 260 nm (at the vertical dashed line) (Figure 2A). The FT-IR spectrum is marked with dashed lines and circles to indicate the absorption peaks. The amino group absorption peaks of PCNLs and TPP-PCNLs are at 3302 cm-1, while the
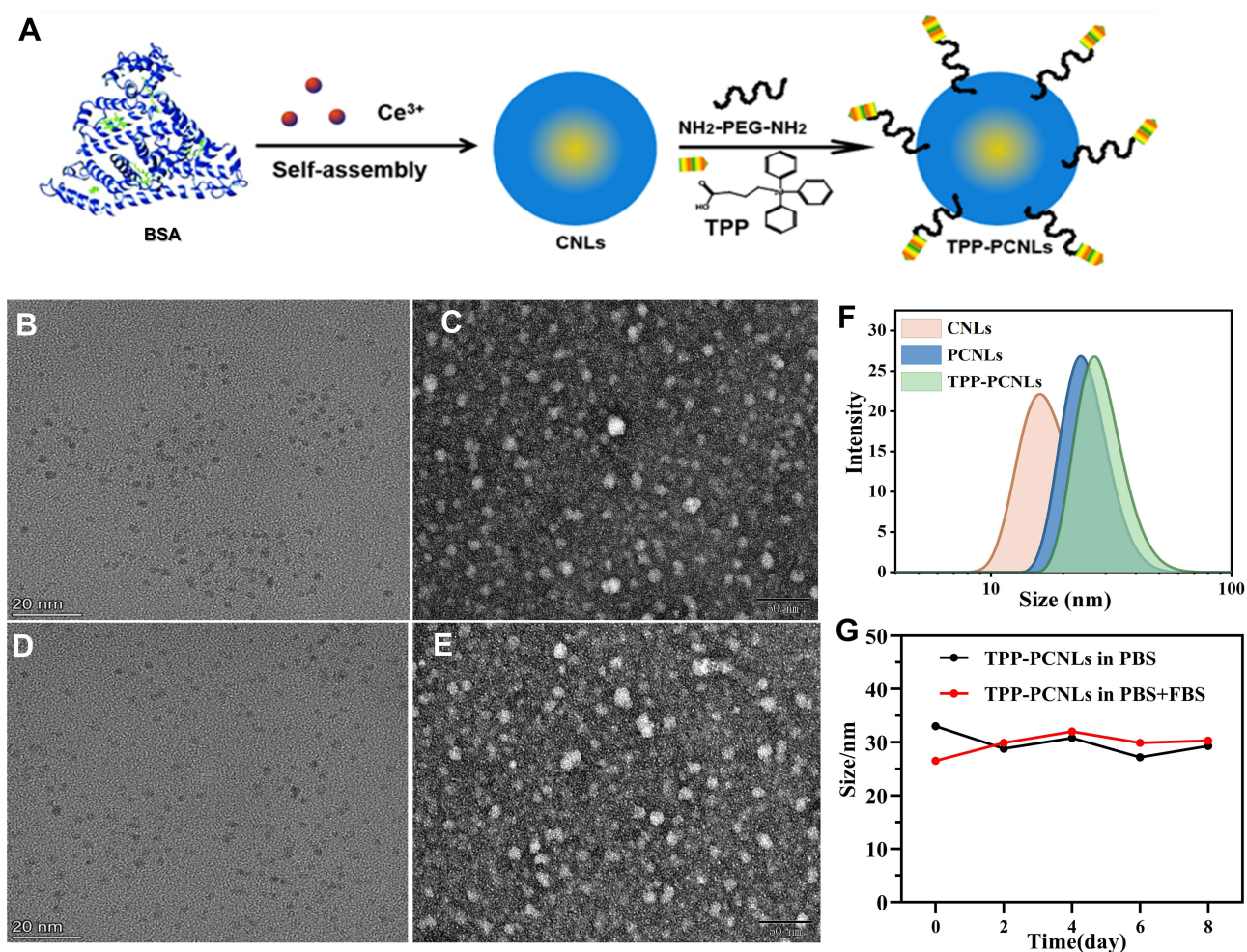
Figure 1 Synthesis and characterization of CNLs, PCNLs and TPP-PCNLs. (**A**) Schematic diagram of the synthesis process of TPP-PCNLs. (**B–E**) HR-TEM, negative staining of tungsten phosphide for PCNLs (**B** and **C**) and TPP-PCNLs (**D** and **E**). (**F**) Hydrated particle size analysis of CNLs, PCNLs and TPP-PCNLs. (**G**) Stability analysis and characterization of TPP-PCNLs by DLS.
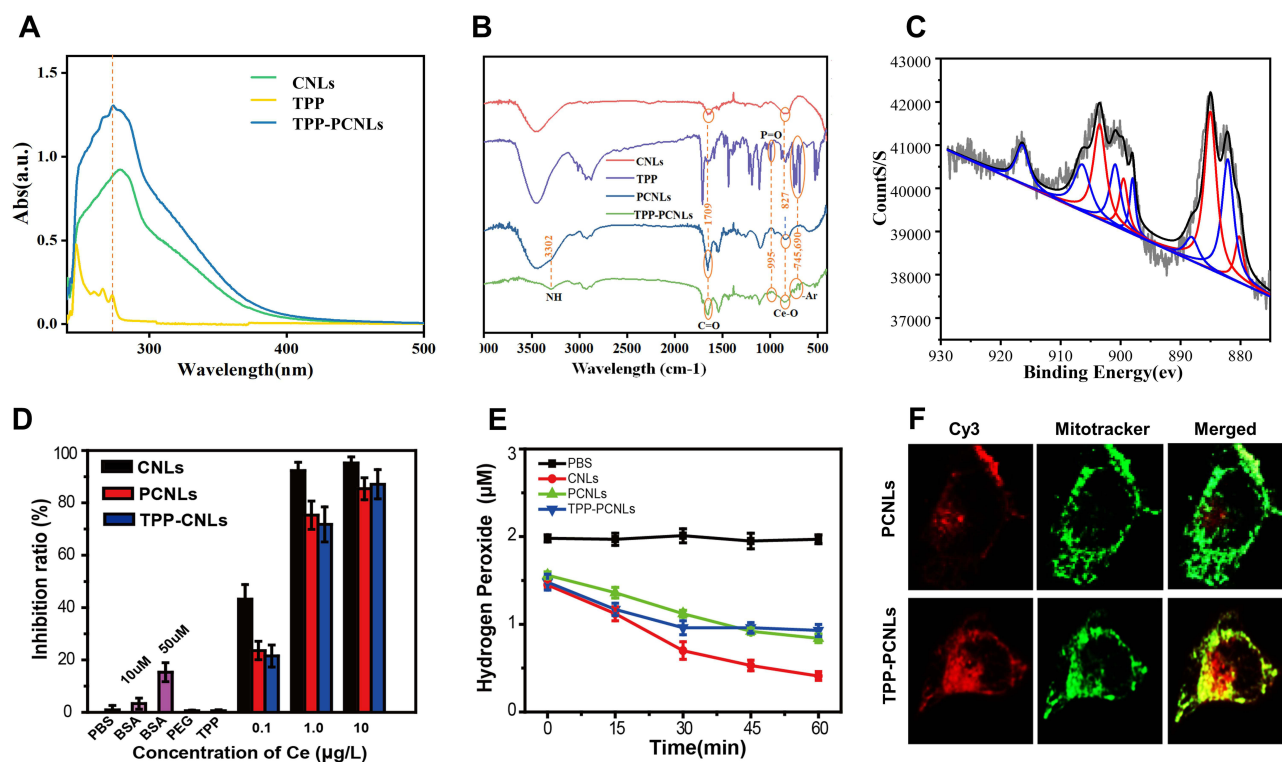
Figure 2 Characterization of CNLs, PCNLs and TPP-PCNLs. (**A**) UV mapping of TPP-PCNLs. (**B**) FTIR spectrum of the CNLs, PCNLs and TPP-PCNLs. (**C**) X-ray Photoelectron Spectroscopy (XPS) of TPP-PCNLs. (**D**) Analysis of SOD activity of CNLs, PCNLs and TPP-PCNLs; (**E**) Analysis of CAT activity. (**F**) Confocal microscopy analysis of PCNLs and TPP-PCNLs and cellular localization analysis with Cy3 amine labeling (red) and Mito-Tracker (green).

C=O and Ce-O absorption peaks of CNLs, PCNLs, and TPP-PCNLs are at 1709 cm-1 and 827 cm-1, respectively. The P=O absorption peak on TPP appears at 745 cm-1 and 690 cm-1 of TPP-PCNLs, the special absorption peaks of the benzene ring (triphenylphosphorus) appear at 745 cm-1 and 690 cm-1 of TPP-PCNLs (Figure 2B). Together, these results validate the successful loading of TPP into PCNLs.

In addition, integrated XPS segment analysis was used to identify the valence state of Ce^{3+} (peaks at 880.20, 885.0, 899.50 and 903.5 eV) and Ce^{4+} (peaks at 882.1, 888.1, 898.0, 900.9, 906.4, and 916.4 eV), validating the presence of mixed valence states (Figure 2C).[11] According to XPS analysis, the Ce^{3+} percentage in the TPP-PCNLs was approximately 50%. As is well known, if ceria nanomaterials have a higher Ce^{3+} to Ce^{4+} ratio, they exhibit more efficiency against diseases induced by ROS or inflammation, because of more oxygen vacancies and higher SOD mimetic activity. Next, SOD analysis of CNLs, PCNLs, and TPP-PCNLs was carried out using the riboflavin light method. The results showed that high-concentration ceria nanoclusters had a high inhibition rate (>90%) on singlet oxygen free radicals, which fully validated the free radical scavenging ability of this type of ceria nanoclusters. However, compared to CNLs, the free radical inhibition rates of PCNLs and TPP-PCNLs decreased slightly (80%) (Figure 2D). Possibly due to the increase in the PEG chain, the contact surface of ceria nanoclusters with free radicals was shielded, leading to a decrease in the free radical inhibition rate; they still maintained a relatively high level, that is, the SOD simulation activity remained at a high level. Additionally, CAT mimetic activity test results were similar to those of the SOD mimetic activity test (Figure 2E). These results showed that cerium nanoclusters had high CAT and SOD mimetic activity.

The results of the animal hemolysis experiment showed that CNLs, PCNLs, and TPP-PCNLs at 0.1, 1, and 10 mg/mL did not show hemolysis, and the hemolysis rate was less than 0, with no statistical difference, indicating that the nanomaterials had good biocompatibility (Figure S1A).

To study the uptake characteristics of PCNLs and TPP-PCNLs by L-02 cells, the ceria content in the cells was determined using ICP-MS at different time points. The results showed that the cellular uptake of nanomaterials reached saturation after 12 h (Figure S1B). Confocal fluorescence microscopy was used to study the colocalization of the PCNLs

and TPP-PCNLs. Ceria nanoclusters were labeled with Cy3 dye to obtain Cy3-PCNLs and Cy3-TPP-PCNLs. The results showed that the fluorescence signals from Mito-tracker (green) matched well with those from Cy3-TPP-PCNLs (red), suggesting that the majority of Cy3-TPP-PCNLs were localized in the mitochondria, as observed by a yellow/orange overlap yield. However, no yellow/orange overlap was observed in cells treated with Cy3-PCNLs, suggesting that Cy3-PCNLs were dispersed in the cytoplasm (Figure 2F). This demonstrated that TPP-PCNLs had a good mitochondrial-targeting effect.

These results indicate that we obtained stable, uniform, and biocompatible ceria nanoclusters (TPP-PCNLs) modified with TPP.TPP- PCNLs have a good ability to clear ROS, simulate CAT and SOD activities, and directly target mitochondria, indicating that they have the ability to target radiation.

In vitro Studies of TPP-PCNLs

Radiation Protection to Cells

Therefore, the safety of PCNLs and TPP-PCNLs was studied. Compared to the control group (0 Gy), there was no significant difference in cell viability between the PCNLs and TPP-PCNLs groups at Ce concentrations from 0.01 to 10 µg/mL ($p \geq 0.05$) (Figure 3A), suggesting that PCNLs and TPP-PCNLs had good biological safety. The protective effects of the PCNLs and TPP-PCNLs were also assessed using a CCK-8 assay. The results showed that compared with the control group, the survival rate of the cells in the radiation group was significantly reduced. In the treatment groups, cell survival was significantly improved in comparison with that in the radiation group at all Ce concentrations. The radioprotective effects of TPP-PCNLs were remarkably higher than those of PCNLs at a Ce concentrations of 0.1–10 µg/mL ($p < 0.05$) (Figure 3B). The protective effect was best when the Ce concentrations was 1µg/ mL.

TPP-PCNLs Target Mitochondria and Affect Morphological Function

TPP is a lipophilic cation that can utilize the negative potential of the mitochondrial membrane to target the mitochondria. Transmission electron microscopy (TEM) analysis showed that the mitochondria in the radiation group had morphological swelling, vacuolar degeneration, and cristae structural changes. The PCNLs treatment group was somewhat condensed and the cristae structure was unclear. The TPP-PCNLs-treated group showed less mitochondrial morphological swelling and a clear cristae structure. TPP-PCNLs showed a certain improvement and maintenance effect on radiation cell morphology (Figure 3C). Moreover, we also confirmed that radiation-induced mitochondrial ATP decline in L-02 cells could be ameliorated by TPP-PCNLs treatment and adjusted the energy supply status of cells; however, PCNLs treatment had no significant improvement effect (Figure 3D). JC-1 forms a polymer and aggregates in the matrix of mitochondria (red fluorescence) when the mitochondrial membrane potential is high. After the membrane potential drops, JC-1 becomes a monomer (green fluorescence) because it cannot aggregates.[12] Compared with the radiation group, the group with 1.0 µg/ mL TPP-PCNLs had a large amount of red fluorescence and a very small amount of green fluorescence, indicating that the MMP was increased significantly (Figure 3E). The results showed that TPP-PCNLs effectively improved MMP damage caused by radiation and maintained mitochondrial membrane integrity, whereas PCNLs did not show any improvement. The Mito-SOX Red kit was used to evaluate superoxide production in the mitochondria of all treatment groups before and after irradiation (Figure 3F). It was suggested that either PCNLs or TPP-PCNLs could efficiently decrease the accumulation of free radicals in the mitochondria of irradiated cells ($P<0.01$). However, PCNLs showed poor efficiency in clearing the accumulation of free radicals in mitochondria. These results suggest that mitochondrial ROS play an important role in radiation-induced damage in L-02 cells. We propose that TPP-PCNLs enter cells and target mitochondria through endocytosis, and their mixed valence state could realize unique redox chemistry and SOD simulation activities and continuously remove reactive oxygen species in cells and mitochondria. TPP-PCNLs effectively improved mitochondrial ATP synthesis, maintained the normal operation of energy, and increased MMP to improve the state of oxidative stress.[12,13]

Therefore, we believe that TPP-PCNLs adjust mitochondrial function and morphology through SOD simulation to protect against radiation.
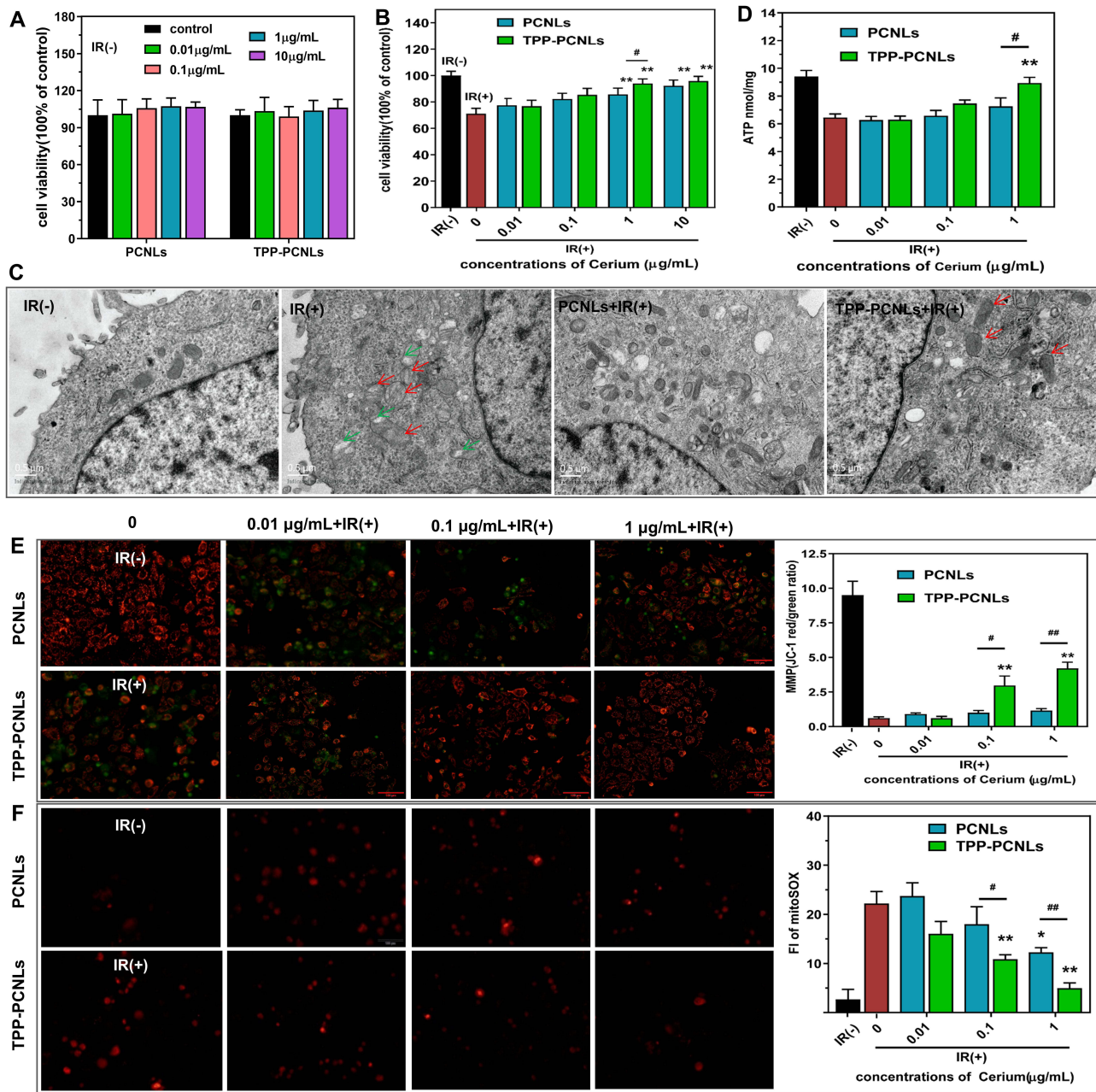
Figure 3 TPP can improve mitochondrial morphology and function damage caused by radiation. (**A**) Effects of PCNLs and TPP-PCNLs on L-02 cell viability. (**B**) Effect of TPP-PCNLs on the survival rate of L-02 cells after 6Gy irradiation. (**C**) ATP energy levels of L-02 cells. (**D**) Transmission electron microscopy (TEM) images of L-02 cells. Mitochondria vacuolization is indicated by an green arrow. (**E**) Fluorescence image and quantitative analysis of the MMP of L-02 cells (100×) detected by the JC-1 method. (**F**) Fluorescence image and quantitative analysis of the Super oxide of L-02 cells (100×) detected by the Mito-SOX method. *Represents a significant difference compared with the IR group, *P<0.05, **P<0.01; #Represents an extremely significant difference compared between PCNLs and TPP-PCNLs, #P<0.05, ##P<0.01.

Radiation Protection Effect of TPP-PCNLs on Cells

To explore the radiation protection mechanism of TPP-PCNLs, a DCFH-DA reactive oxygen detection kit was used to analyze the ROS levels before and after irradiation. The results showed that TPP-PCNLs significantly reduced the level of ROS in the cytoplasm induced by radiation (p < 0.01), whereas PCNLs only slightly alleviated ROS levels (Figure 4A).

The monoclonal experiment showed that compared with the normal group, the formation of L-02 cell colonies was significantly reduced in the irradiated group (59 colonies). Compared with the radiation group, the number of colonies in
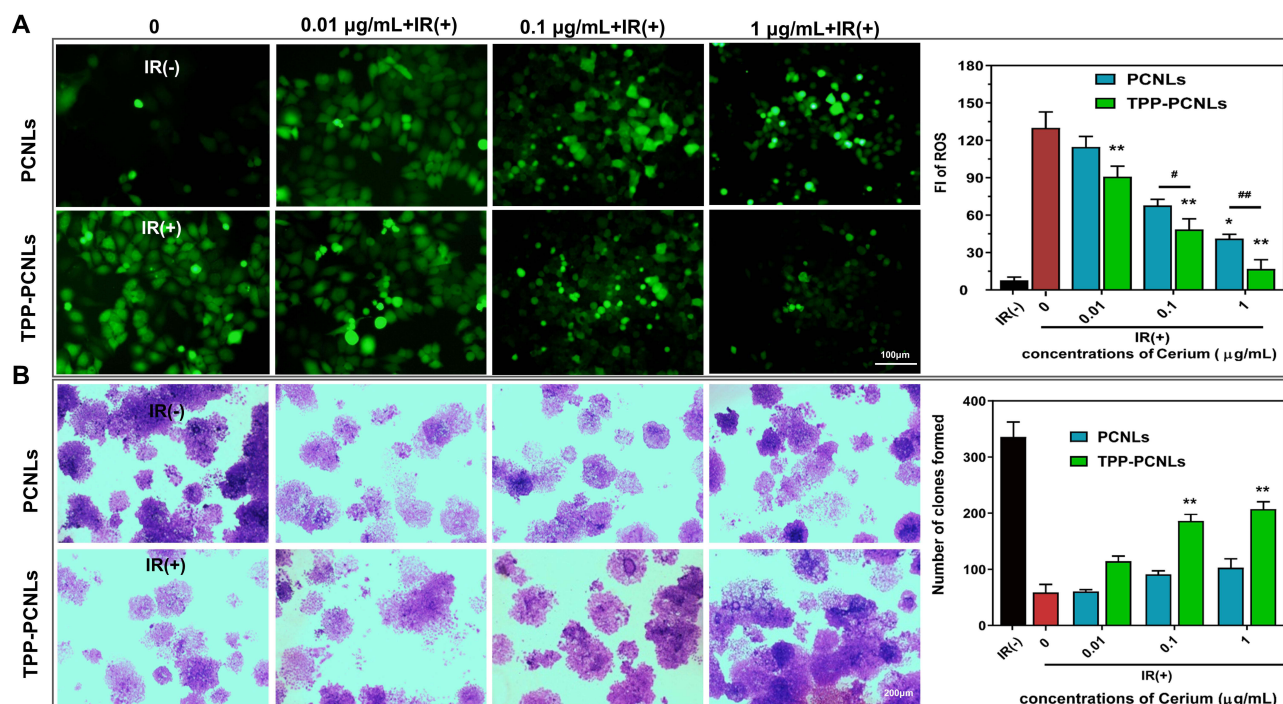
Figure 4 Radioprotection effect of TPP-PCNLs in irradiated cells. Images and quantitative analysis of L-02 cells treated with PCNLs and TPP-PCNLs. (**A**) Fluorescence image of the ROS of L-02 cells (100×) detected by the DCFH-DA method. (**B**) Image of cell colony formation. L-02 cells were pretreated with TPP-PCNLs, and colony formation was examined 10 days after 6Gy irradiation (40×). *Represents a significant difference compared with the IR group, *$P<0.05$, **$P<0.01$; #Represents an extremely significant difference compared between PCNLs and TPP-PCNLs, #$P<0.05$, ##$P<0.01$.

the TPP-PCNLs group (207 colonies) increased significantly ($P<0.05$), but those in the PCNLs group (103 colonies) did not change significantly ([Figure 4B](#)). The radioprotective effects of TPP-PCNLs on L-02 cells were further verified by Calcein AM and propidium iodide co-staining. Therefore, compared with PCNLs, TPP-PCNLs improved radiation-induced cell damage ([Figure S2](#)) (p < 0.05).

Comet electrophoresis was used to study the nuclear DNA damage and radiation resistance mechanisms of the TPP-CNLs. Compared with the PCNLs group, the TPP-PCNLs group effectively inhibited the trailing phenomenon caused by DNA damage, 37% of the comet trail in the irradiation group and 14.6% in the 1.0μg/mL TPP-PCNLs treatment group, which reduces the damage of secondary free radicals to nuclear DNA indirectly by 22.45% ([Figure 5A](#)).

Apoptosis is the process of programmed cell death[13] mitochondrion is a key subcellular compartment, in which apoptosis is intimately associated with ROS generation and oxidative stress.[14]

Radiation-induced damage can cause ROS overload, which triggers apoptosis.[15]

The results of flow cytometry showed that the early and late apoptosis rates (12.78%) of the cells in the 0.1μg/mL TPP-PCNLs group were significantly decreased compared with the irradiation group (21.7%) (p < 0.05) ([Figure S3](#)). The apoptosis rate (4.24%) in the 1.0μg/mL TPP-PCNLs group. These results suggest that the higher the dose of TPP-PCNLs, the lower is the apoptosis rate. In short, TPP-PCNLs can effectively maintain the integrity and function of the mitochondria and provide the necessary guarantee for nuclear DNA repair and damage repair in cells.

Western blotting was performed to analyze the expression of apoptosis-related proteins. Compared with the normal group, the expression of apoptosis-related proteins caspase-3, caspase-9, and the pro-apoptotic factor BAX increased in the irradiated group ($P<0.01$), whereas the expression of apoptosis-inhibiting factor Bcl-2 decreased, this indicates that radiation causes oxidative damage to L-02, activating the caspase signaling pathway. Compared with the irradiation group, the expression of caspase-3, caspase-9, and Bax in the TPP-PCNLs group was downregulated, and the expression of Bcl-2 was up-regulated ($P<0.05$), TPP-PCNLs improved radiation induced changes in apoptosis related proteins ([Figure 5C](#)).
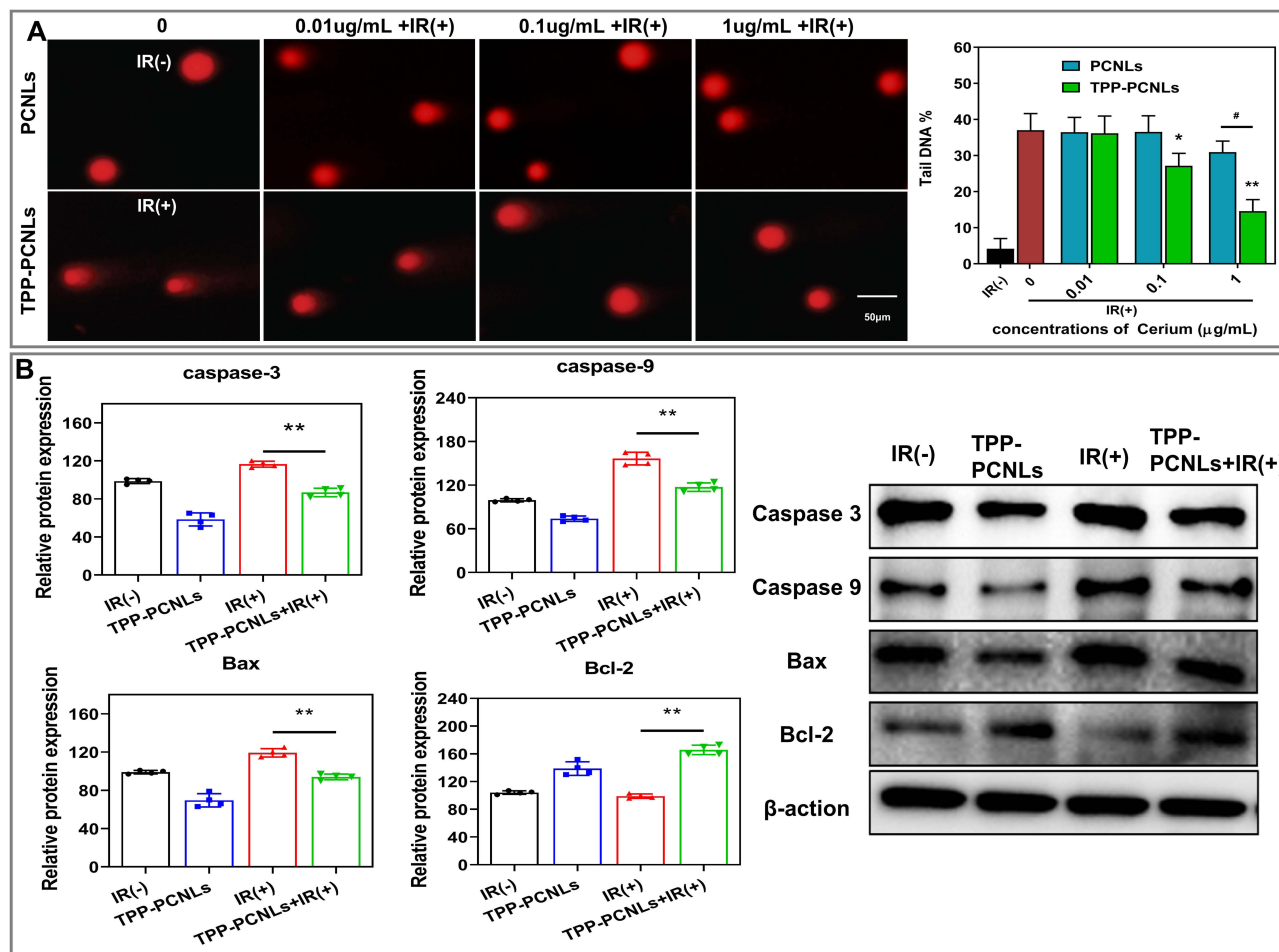
Figure 5 Cellular mechanism of radiation protection of TPP-PCNLs. (**A**) Comet image of DNA damage in L-02 cells (100×). (**B**) Detection and quantitative analysis of apoptosis-related protein expression in irradiated L-02 cells treated with TPP-PCNLs. *$P<0.05$ vs IR (+), **$P<0.01$ vs IR (+).

In vivo Study of Anti-Radiation Effects of TPP-PCNLs

Mouse Imaging in vivo

The results showed that ICG was quickly cleared after 8h. However, PCNLs and TPP-PCNLs loaded with ICG were distributed throughout the body within 0–24h, their residence time in vivo was significantly extended. They accumulated to a greater extent in the extramedullary hematopoietic tissues, such as the liver and spleen, even after 24h of administration. This indicated that TPP-PCNLs loading improved the efficiency of drug action in the body and prolonged the duration of drug action (Figure S4).

Bio-Distribution

The cerium content in the blood of mice treated with the cerium nanomaterials was analyzed using ICP-MS. Compared to CNLs, TPP-PCNLs and PCNLs had significantly longer blood circulation times and higher Ce concentrations (Figure 6A). At 2–12 hours, there was no significant difference in blood distribution between the TPP-PCNLs and PCNLs. The Ce content in the liver and spleen of the three experimental groups was higher than that in the other tissues, and the Ce content in the TPP-PCNLs group was higher than that in the PCNLs group (Figure 6B). These results indicate that the liver and spleen are the main aggregation sites of cerium dioxide nanoclusters and are the key sites of extramedullary hematopoiesis, which plays an important role in the anti-radiation effect.
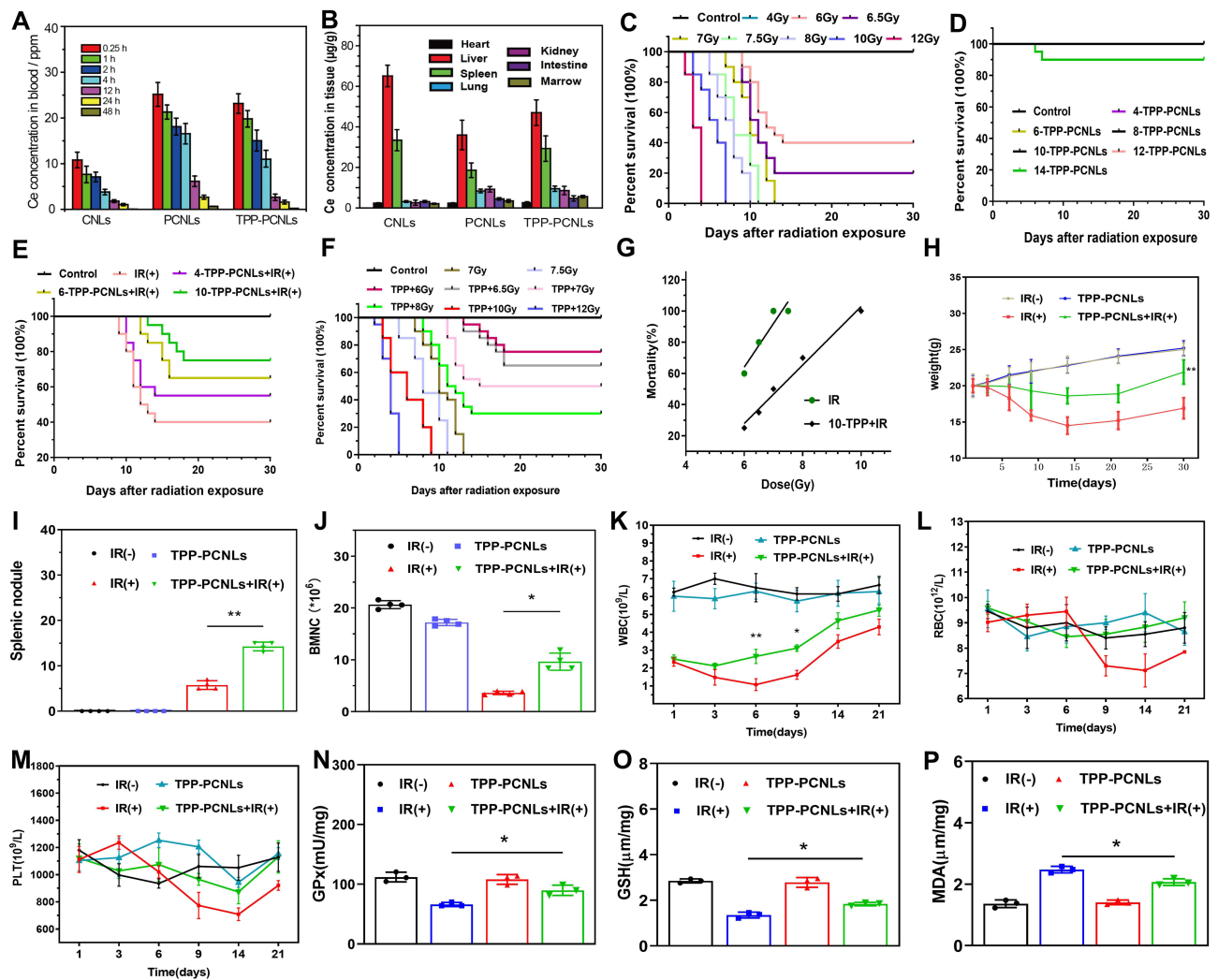
Figure 6 Radioprotection effect of TPP-PCNLs in vivo. (**A**) Changes in ceria content in the blood of mice at different time points after CNLs, PCNLs and TPP-PCNLs treatment. (**B**) Changes in ceria content in the heart, liver, spleen, lungs and kidneys of mice after CNLs, PCNLs and TPP-PCNLs treatment. (**C–G**) Assessment of radioprotective effect of TPP-PCNLs on WBI mice. (**H**) Weight of the mice in each group. (**I and J**) Splenic nodules. The nucleated cells in bone marrow were counted. (**K–M**) Changes in red blood cell counts (RBCs), white blood cell counts (WBCs) and platelets (PLTs) in the peripheral blood of mice at different time points. (**N–P**) Levels of glutathione peroxidase (GP-x), malondialdehyde (MDA) and glutathione (GSH) in the serum of the mice in each group. *Represents a significant difference compared with the IR group, *$P<0.05$, **$P<0.01$.

Evaluation of Radiation Protection Effect and Hematopoietic Function

Determination of DRF Value for TPP-PCNLs

Administration of TPP-PCNLs improved the survival rate of BALB/c mice after lethal whole-body irradiation (WBI). To better evaluate whether TPP-PCNLs had a therapeutic effect on radiation-damaged mice, the effects of different radiation doses (4, 6, 6.5, 7, 7.5, 8, 10 and 12 Gy) on the 30-day survival rate of BALB/c mice were evaluated. The survival rate of BALB/ C mice was only 40% after 6 Gy X-ray irradiation. Therefore, 6 Gy was selected as the optimal dose for the survival analysis (Figure 6C). The LD50/30 ratio of mice in the radiation group was estimated to be 5.5 Gy, based on the dose-survival curve of irradiation. The group treated with 4–12 mg/kg TPP-PCNLs alone showed no toxicity in BALB/c mice (Figure 6D). According to previous experimental results, most TPP-PCNLs accumulate in extramedullary hematopoietic organs, such as the liver and spleen after 12h of caudal vein injection, exerting an anti-radiation effect. At 12h before irradiation (8 Gy), pretreatment with 4, 6 and 10 mg/kg TPP-PCNLs increased the survival rate by approximately 15, 25 and 35% (compared with IR, respectively ($p < 0.05$). Therefore, the optimal dose of TPP-PCNLs was determined to be 10 mg/kg (Figure 6E). Pre-treatment with 10 mg/kg TPP-

PCNLs was followed by irradiation at different doses (6, 6.5, 7, 8, 10 and 12 Gy). The LD50/30 of 10 mg/kg TPP-PCNLs in the irradiated mice was 7.2 Gy (Figure 6F). The anti-radiation ability of the TPP-PCNLs was determined using the DRF value. According to formula (1), LD50/30 (TPP-PCNLs) is 7.2 Gy, and the radiation group LD50/30 is 5.5 Gy, then the DRF is 1.30 (10 mg/kg) (Figure 6G), which indicates that TPP-PCNLs has a good radiation protection effect.

The weight of the mice in the normal and TPP-PCNLs groups increased gradually over time. The weight of mice in the IR (+) group decreased to a minimum of approximately 14 g on the 11th day, and then gradually increased. The weights of the mice in the TPP-PCNLs + IR (+) group were higher than those in the IR (+) group. Similar to the control group, mice in the TPP-PCNLs group did not die within 30 days, indicating no biological toxicity (Figure 6H).

The liver and spleen are the main hematopoietic organs other than the bone marrow, and are also the main sites for the accumulation of cerium dioxide nanoclusters. CFU-S represents hematopoietic stem cells that can differentiate into myeloid and lymphoid cells.[16] The number of splenic nodules in mice was observed on the 8th day after radiation exposure. The number in the IR group was lower, whereas the number in the TPP-PCNLs + IR (+) group was the highest, with a significant difference ($P < 0.05$) (Figure 6I), indicating that TPP-PCNLs could significantly enhance the hematopoietic function of the spleen after radiation injury. Similarly, the number of nucleated cells in the bone marrow decreased sharply in the IR (+) group, while that in the TPP-PCNLs +IR (+) group was significantly higher than that in the other groups (Figure 6J), further indicating that TPP-PCNLs significantly enhanced the hematopoietic ability in the bone marrow.

The effect of TPP-PCNLs on peripheral blood cell proliferation after irradiation was also examined. Compared with the IR (-) group, there was no significant difference in the number of leukocytes in the TPP-PCNLs group. The number of leukocytes in the IR (+) group decreased on day 6 after irradiation and reached its lowest level on day 9. Compared to the IR (+) group, the number of leukocytes in the TPP-PCNLs + IR (+) group was significantly increased on days 6 and 9 ($P < 0.05$) and increased to the normal level on 21st days (Figure 6K), indicating that TPP-PCNLs have a good radiation protection effect.The RBC and platelet counts were not significantly different between the treatment groups ($P > 0.05$) (Figure 6L and M).[17]

The expression levels of GSH, glutathione peroxidase (GP-x), and MDA lipid peroxidation in liver tissue were measured to determine the anti-radiation mechanism of TPP-PCNLs. Compared to the control group, the expression level of MDA in the IR group increased, whereas the levels of GSH and GP-x decreased. The TPP-PCNLs +IR (+) group effectively reduced the expression level of MDA, improved the level of GSH and GP-x induced by radiation ($P < 0.05$) (Figure 6N–P), enhanced the body's ability to resist free radicals, inhibited the excessive oxidation reaction, and had obvious antioxidant effects.

Hematoxylin-Eosin Staining

HE staining results showed that no pathological morphological changes were observed in any organ in the TPP-PCNLs group (Figure S5), proving that TPP-PCNLs had good biosafety. The radiation protection effect of ceria nanoclusters was observed for 3 days from the point of view of pathophysiology. Radiation-sensitive bone marrow tissue was damaged after irradiation. Compared with the control, in the IR (+) group, the number of hematopoietic cells in the bone marrow decreased, a large number of mature red blood cells were filled, hematopoietic function was low, and the number of nuclear cells and lymphocytes decreased dramatically. Compared to the IR (+) group, the number of hematopoietic cells in the TPP-PCNLs +IR (+) group was significantly increased, effectively maintaining the number of hematopoietic cells and preventing radiation-induced bone marrow injury (Figure 7A). 6 Gy radiation causes the small intestinal villi to shrink and fall. The villi were arranged irregularly and local crypt cells were infiltrated by inflammation. Compared with the IR (+) group, the small intestinal villi in the TPP-PCNLs + IR group were longer, and the villus structure was more intact, indicating that radiation damage to the small intestine could be prevented (Figure 7B). With radiation alone, the hepatic sinuses were observably enlarged, accompanied by obvious vacuolation, partial apoptosis, and necrosis of liver cells, partial apoptosis and inflammatory infiltration of spleen cells, decreased hematopoietic cells and lymphocytes in the spleen, inflammatory infiltration, and unclear demarcation of the cortex and medulla. The TPP-PCNLs + IR (+) group effectively alleviated these pathological changes and maintained the normal structure of the liver and spleen (Figure 7C
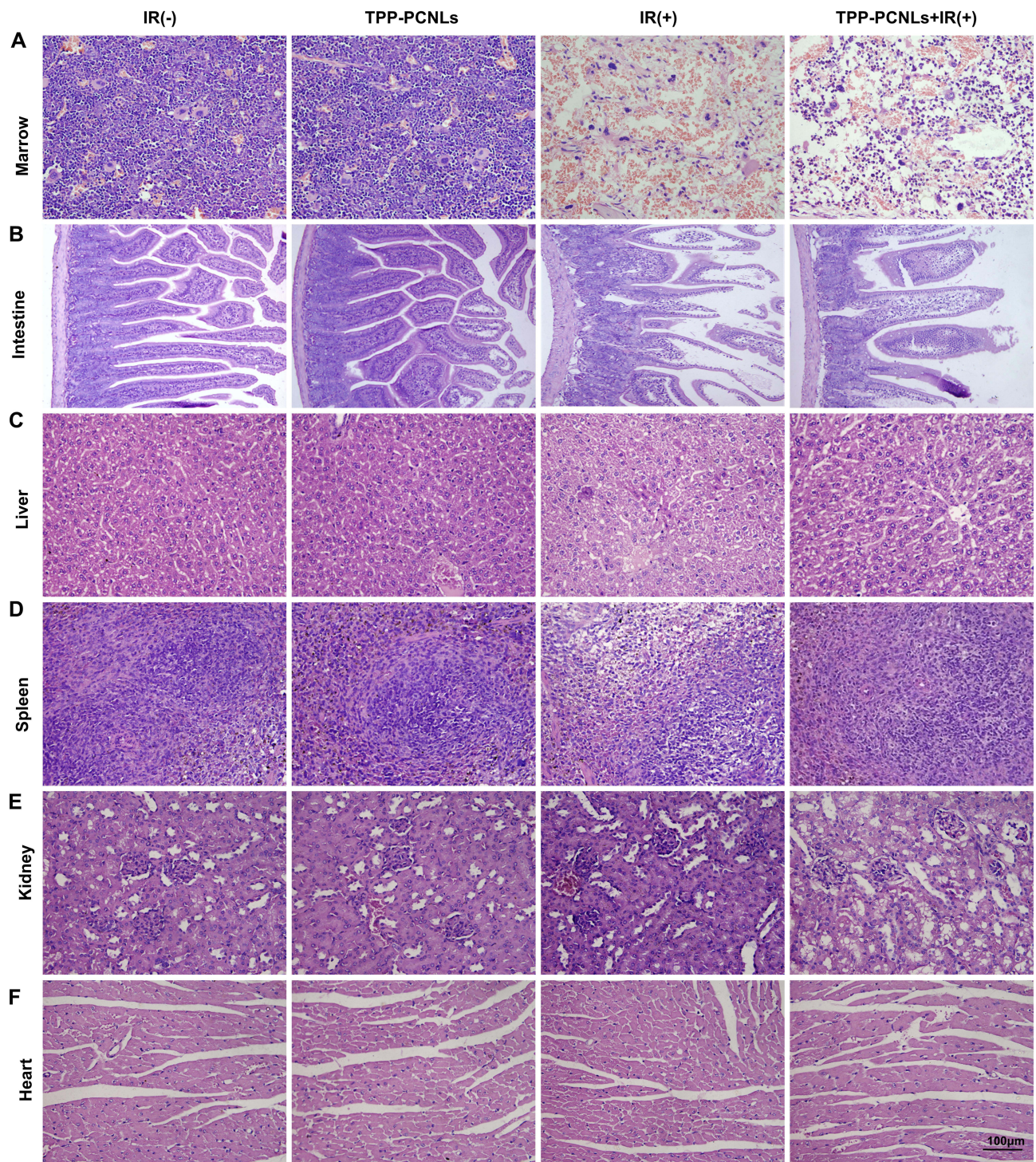
Figure 7 Histopathological changes in the bone marrow (**A**), small intestine (**B**), liver (**C**), spleen (**D**), kidney (**E**) and heart (**F**) in each group were evaluated by hematoxylin and eosin (H&E) staining.

and D). The TPP-PCNLs + IR (+) group could prevent the edema phenomena of renal tubular epithelial cells caused by radiation, the unclear cell boundary, and the disorder and irregularity phenomena of renal tubules and epithelial cells (Figure 7E). TPP-PCNLs also improved the loose arrangement of cardiomyocytes (Figure 7F).

The pathological morphology of the bone marrow in each group was observed seven days after irradiation. Compared to the IR (+) group, the number of hematopoietic cells in the TPP-PCNLs +IR (+) group was significantly increased,

mature red blood cells were significantly reduced, and hematopoietic function was significantly improved. TPP-PCNLs effectively enhanced the hematopoietic capacity and reduced radiation-induced bone marrow damage (Figure S6).

In conclusion, there was no difference in routine blood and pathological morphology between the TPP-PCNLs and the normal control group, and the whole-body performance was good, indicating that the biosafety of TPP-PCNLs was good. TPP-PCNLs, which mainly accumulate in radiation-sensitive tissues such as the liver and spleen, have multifunctional enzymatic activity and target mitochondria, enabling them to continuously cycle and eliminate ROS. TPP-PCNLs can improve oxidative stress in the mitochondrial pathway, reduce cell apoptosis, improve the survival rate of irradiated mice, significantly improved hematopoietic recovery in mice, and provide mitochondria-targeted radiation protection.

Discussion

We performed PEG-mediated BSA targeting of mitochondria using TPP and grafted it onto a multifunctional cerium nanocluster system (CNLs) with controllable enzymatic activity. We synthesized a TPP-PCNLs that targets mitochondria to continuously clear ROS. The size of TPP-PCNLs is about 2nm, and the hydrated particle size is about 30nm. Due to the valence distribution ratio of Ce^{3+}/Ce^{4+} and high oxygen vacancies, it has high SOD mimetic enzyme activity, and an efficiently clear ROS. Compared to PCNLs, TPP-PCNLs can effectively enhance the chemical stability and biocompatibility of nanomaterials, and at the same time, they have high efficiency, selectivity, and renewability for scavenging free radicals and target mitochondria for sustained action. Through cell and animal experiments, it was confirmed that TPP-PCNLs have significant anti-radiation effects, and their mechanisms were elucidated.

TPP-PCNLs efficiently simulated the activity of SOD and removed free radicals produced by radiation. At the same Ce concentration, the SOD activity of the CNLs was higher due to its extremely high specific surface area than that of the CNHs and CNPs. Among the two main oxides of cerium oxide (Ce^{3+} and Ce^{4+}), BSA with reductive disulfide bonds becomes a nanoreactor and grows directly into cerium nanoclusters by forming Ce-BSA complexes.[8] Xu, P.T. also demonstrated that PCNPs had significant clinical and histological improvements in radioactive lung injury induced by lethal dose radiation. This is because PCNPs provide an active site for free radical scavenging, and their mixed valence state can achieve unique CAT activity and SOD simulation activity and realize the renewable ability of free radical scavenging.[17]

Linking PEG with CNLs and BSA as a carrier and controlled-release agent enhances biocompatibility and stability. Cerium-based nanostructures must maintain broad biocompatibility and prevent systemic toxicity to normal cells and tissues.[18] CNPs without adequate surface protection can accumulate and be cleared by the reticuloendothelial system, resulting in poor biomedical performance, so the surface of nanoparticles needs to be protected and modified.[18] As a hydrophilic polymer, PEG chains are most effective in tailoring surface properties such as surface charge, biocompatibility, and solubility.[19–21] It has been shown that PEG600-coated CNPs improve SOD activity, prolong blood circulation time, exhibit excellent dispersion properties in cells, and stabilize in a range of physiological solutions, indicating that PEG can easily stabilize cerium nanoparticles.[9] In the dose range studied, TPP-PCNLs has good biocompatibility and stability, and has no cytotoxicity to L-02.

By targeting the mitochondria, TPP-PCNLs reduce ROS production and alleviate secondary free radical damage to the nuclear DNA. Compared to nuclear DNA, mtDNA is more sensitive to radiation and free radical damage owing to a lack of histone protection and effective self-repair. There is a higher chance of adverse effects due to mtDNA deletion. After irradiation, the damaged mtDNA is unable to repair itself but continues to replicate the damage, resulting in an increase in the number of damaged mtDNA.[22,23] This further causes mitochondrial dysfunction, resulting in oxidative stress responses and ROS production. Free radicals produced by mitochondria can enter the nucleus and cause sustained secondary free radical damage to nuclear DNA. It is speculated that TPP-PCNLs can reduce the ROS increase caused by mtDNA overexpression by targeting the mitochondria and play an important role in repairing nuclear DNA damage.

TPP-PCNLs improved MMP and ATP levels and decreased the apoptosis rate. Radiation can significantly increase mtDNA, affect ATP synthesis and oxidative phosphorylation processes, damage mitochondrial function, and lead to apoptosis. By targeting mitochondria, TPP-PCNLs can better transport drugs to the mitochondria, increase MMP and ATP levels of cells, and further reduce cell apoptosis after exposure. Pourkhalili et al found that cerium nanoparticles can increase the ratio of ATP/ADP in the mitochondria and enhance the levels of ATP and MMP, thereby playing an important role in inhibiting apoptosis.[3,24,25]

TPP-PCNLs may play an anti-radiation role by inhibiting apoptosis through the mitochondrial pathway. ROS produced by radiation causes the opening of transitional pores of mitochondrial membrane permeability, changes the structure of the membrane system, and leads to apoptosis of mitochondrial pathway cells.[26] Bcl-2/ BAX mainly shows regulatory effects on mitochondrial permeability, membrane potential, and caspase family proteins. After receiving the apoptotic signal, mitochondria release apoptotic factors, including cytochrome c apoptosis-inducing factor (AIF), which binds to caspase-9, resulting in its own cleavage and activation, and further activates downstream caspase-3, leading to apoptosis.Through targeting mitochondria, TPP-PCNLs may reduce ROS levels, increase the Bcl-2/BAX ratio, inhibit the expression of homologous activated and apoptosis-inducing Caspase −9, inhibit the apoptosis of the mitochondrial pathway, and further inhibit the expression of heterologous activated Caspase-3, thereby reducing the apoptosis rate.[27–30] Radiation causes oxidative stress damage to L-02 cells, activating the Caspase apoptotic signaling pathway. TPP-PCNLs can effectively alleviate this oxidative damage by targeting mitochondria, significantly inhibiting the Caspase apoptotic signaling pathway, and reducing the expression of caspase-3 and 9. And it increases the upstream protein Bcl-2 and decreases BAX, enhances antioxidant capacity, improves radiation damage, and thus protects cells.

Conclusion

In this study, mitochondria-targeted ceria nanoclusters (TPP-PCNLs) with good biocompatibility were obtained via PEGylation-mediated mitochondrial-targeted molecular modification. The size of TPP-PCNLs is only 2nm and the unique coexistence of Ce^{3+} and Ce^{4+}. TPP-PCNLs can target mitochondria to continuously clear free radicals, efficient simulation of SOD enzyme activity and improving oxidative stress status in vitro and in vivo, maintaining mitochondrial function and morphology, and exert a protective effect by regulating the mitochondrial apoptosis pathway, reduce DNA damage and cell apoptosis. TPP-PCNLs mainly accumulate in radiation-sensitive tissues such as the liver and spleen, improve the survival rate of irradiated mice, significantly improved hematopoietic recovery in mice and achieve radiation protection. Our results demonstrate that TPP-PCNLs can be used in the development of radiation protection strategies and have potential applications. Finally, this new strategy may be a candidate for improving the patients' quality of life and ameliorating the late effects of radiation damage in the future.

Abbreviations

TPP-PCNLs, albumin-cerium oxide nanoclusters; TPP, triphenyl phosphate; DRF, dose reduction factor; ROS, reactive oxygen species; IR, ionizing Radiation; ATP, adenosine triphosphate; SOD, superoxide dismutase; MMP, mitochondrial membrane potential; CNLs, cerium dioxide nanoclusters; CNPs, cerium dioxide nanoparticles; CNHs, cerium dioxide nanochains; PEG, polyethylene glycol; DMSO, dimethyl sulfoxide; XPS, X-ray photoelectron spectroscopy; MDA, malondialdehyde; RBCs, red blood cells; WBCs, white blood cells; PLTs, platelets; BMNCs, bone marrow nuclear cells; CFU-S, count of splenic nodules; DLS, dynamic light scattering; BSA, bovine serum albumin; CAT, catalase; TEM, transmission electron microscopy; PI, propidium iodide; WB, Western blotting; ICG, indocyanine green; GP-x, glutathione peroxidase; AIF, apoptosis-inducing factor; TEM, transmission electron microscope; WBI, whole-body irradiation.

Acknowledgments

Disclosure

The authors report no conflicts of interest in this work.

References

1. Kamran MZ, Ranjan A, Kaur N, et al. Radioprotective Agents: strategies and Translational Advances. *Med Res Rev.* 2016;36(3):461–493. doi:10.1002/med.21386

2. Richter C, Park JW, Ames BN. Normal oxidative damage to mitochondrial and nuclear DNA is extensive. *Proc Natl Acad Sci USA.* 1988;85 (17):6465–6467. doi:10.1073/pnas.85.17.6465

3. Pourkhalili N, Hosseini A, Nili-Ahmadabadi A, et al. Improvement of isolated rat pancreatic islets function by combination of cerium oxide nanoparticles/sodium selenite through reduction of oxidative stress. *Toxicol Mech Methods.* 2012;22(6):476–482. doi:10.3109/15376516.2012.673093

4. Yu H, Jin F, Liu D, et al. ROS-responsive nano-drug delivery system combining mitochondria-targeting ceria nanoparticles with atorvastatin for acute kidney injury. *Theranostics.* 2020;10(5):2342–2357. doi:10.7150/thno.40395

5. Wang Z, Shen X, Gao X, et al. Simultaneous enzyme mimicking and chemical reduction mechanisms for nanoceria as a bio-antioxidant: a catalytic model bridging computations and experiments for nanozymes. *Nanoscale.* 2019;11(28):13289–13299. doi:10.1039/c9nr03473k

6. Singh S, Dosani T, Karakoti AS, et al. A phosphate-dependent shift in redox state of cerium oxide nanoparticles and its effects on catalytic properties. *Biomaterials.* 2011;32(28):6745–6753. doi:10.1016/j.biomaterials.2011.05.073

7. Wang H, Wang L, Chen Y, et al. Catalytically proficient ceria nanodots supported on redox-active mesoporous hosts for treatment of inflammatory bowel disease via efficient ROS scavenging. *J Mater Chem B.* 2023;11(43):10369–10382. doi:10.1039/d3tb01602a

8. Yang Z, Luo S, Zeng Y, et al. Albumin-mediated biomineralization of shape-controllable and biocompatible ceria nanomaterials. *ACS Appl Mater Interfaces.* 2017;9(8):6839–6848. doi:10.1021/acsami.6b15442

9. Li H, Yang ZY, Liu C, et al. PEGylated ceria nanoparticles used for radioprotection on human liver cells under γ-ray irradiation. *Free Radic Biol Med.* 2015;87:26–35. doi:10.1016/j.freeradbiomed.2015.06.010

10. Park EJ, Choi J, Park YK, et al. Oxidative stress induced by cerium oxide nanoparticles in cultured BEAS-2B cells. *Toxicology.* 2008;245(1–2):90–100. doi:10.1016/j.tox.2007.12.022

11. Gupta A, Das S, Neal CJ, et al. Controlling the surface chemistry of cerium oxide nanoparticles for biological applications. *J Mat Chem B.* 2016;4 (19):3195–3202. doi:10.1039/C6TB00396F

12. Kwon HJ, Kim D, Seo K, et al. Ceria nanoparticle systems for selective scavenging of mitochondrial, intracellular, and extracellular reactive oxygen species in parkinson's disease. *Angew Chem Int Ed Engl.* 2018;57(30):9408–9412. doi:10.1002/anie.201805052

13. Li Y, Hou X, Yang C, et al. Photoprotection of cerium oxide nanoparticles against UVA radiation-induced senescence of human skin fibroblasts due to their antioxidant properties. *Sci Rep.* 2019;9(1):2595. doi:10.1038/s41598-019-39486-7

14. Sinha K, Das J, Pal PB, et al. Oxidative stress: the mitochondria-dependent and mitochondria-independent pathways of apoptosis. *Arch Toxicol.* 2013;87(7):1157–1180. doi:10.1007/s00204-013-1034-4

15. Uğuz AC, Nazıroğlu M, Espino J, et al. Selenium modulates oxidative stress-induced cell apoptosis in human myeloid HL-60 cells through regulation of calcium release and caspase-3 and −9 activities. *J Membr Biol.* 2009;232(1–3):15–23. doi:10.1007/s00232-009-9212-2

16. Necas E, Znojil V, Sefc L. Haemopoietic stem cells: spleen colony-forming cells are normally actively proliferating. *Cell Tissue Kinet.* 1990;23 (6):637–649. doi:10.1111/j.1365-2184.1990.tb01351.x

17. Xu PT, Maidment BR, Antonic V, et al. Cerium Oxide Nanoparticles: a Potential Medical Countermeasure to Mitigate Radiation-Induced Lung Injury in CBA/J Mice. *Radiat Res.* 2016;185(5):516–526. doi:10.1667/RR14261.1

18. Poon W, Zhang YN, Ouyang B, et al. Elimination Pathways of Nanoparticles. *Acs Nano.* 2019;13(5):5785–5798. doi:10.1021/acsnano.9b01383

19. Saifi MA, Seal S, Godugu C. Nanoceria, the versatile nanoparticles: promising biomedical applications. *J Control Release.* 2021;338:164–189. doi:10.1016/j.jconrel.2021.08.033

20. Yadav S, Chamoli S, Kumar P, et al. Structural and functional insights in polysaccharides coated cerium oxide nanoparticles and their potential biomedical applications: a review. *Int J Biol Macromol.* 2023;246:125673. doi:10.1016/j.ijbiomac.2023.125673

21. Karakoti AS, Das S, Thevuthasan S, et al. PEGylated inorganic nanoparticles. *Angew Chem Int Ed Engl.* 2011;50(9):1980–1994. doi:10.1002/anie.201002969

22. Zhou X, Li N, Wang Y, et al. Effects of X-irradiation on mitochondrial DNA damage and its supercoiling formation change. *Mitochondrion.* 2011;11(6):886–892. doi:10.1016/j.mito.2011.07.005

23. Carvalho G, Repolês BM, Mendes I, et al. Mitochondrial DNA Instability in Mammalian Cells. *Antioxid Redox Signal.* 2022;36(13–15):885–905. doi:10.1089/ars.2021.0091

24. Pourkhalili N, Hosseini A, Nili-Ahmadabadi A, et al. Biochemical and cellular evidence of the benefit of a combination of cerium oxide nanoparticles and selenium to diabetic rats. *World J Diabetes.* 2011;2(11):204–210. doi:10.4239/wjd.v2.i11.204

25. Hosseini A, Baeeri M, Rahimifard M, et al. Antiapoptotic effects of cerium oxide and yttrium oxide nanoparticles in isolated rat pancreatic islets. *Hum Exp Toxicol.* 2013;32(5):544–553. doi:10.1177/0960327112468175

26. Thakur RS, Devaraj E. Lagerstroemia speciosa (L.) Pers. triggers oxidative stress mediated apoptosis via intrinsic mitochondrial pathway in HepG2 cells. *Environ Toxicol: Int J.* 2020;35(11):1225–1233. doi:10.1002/tox.22987

27. Kaloni D, Diepstraten ST, Strasser A, Kelly GL. BCL-2 protein family: attractive targets for cancer therapy. *Apoptosis.* 2023;28(1–2):20–38. doi:10.1007/s10495-022-01780-7

28. Mohan S, Abdelwahab SI, Kamalidehghan B, et al. Involvement of NF-κB and Bcl2/Bax signaling pathways in the apoptosis of MCF7 cells induced by a xanthone compound Pyranocycloartobiloxanthone A. *Phytomedicine.* 2012;19(11):1007–1015. doi:10.1016/j.phymed.2012.05.012

29. Vucicevic K, Jakovljevic V, Colovic N, et al. Association of bax expression and Bcl2/Bax ratio with clinical and molecular prognostic markers in chronic lymphocytic leukemia. *J Med Biochem.* 2016;35(2):150–157. doi:10.1515/jomb-2015-0017

30. Swanton E, Savory P, Cosulich S, et al. Bcl-2 regulates a caspase-3/caspase-2 apoptotic cascade in cytosolic extracts. *Oncogene.* 1999;18 (10):1781–1787. doi:10.1038/sj.onc.1202490